The effect of pore structure on the permeability of tight sandstones

G. CHEN[1], J. BA[1], H. ZHU[1], J.M. CARCIONE[1, 2] AND L. GAO[1]

[1] School of Earth Sciences and Engineering, Hohai University, Nanjing, China
[2] National Institute of Oceanography and Applied Geophysics – OGS, Trieste, Italy

ABSTRACT The estimation of permeability is essential as it is closely related to the production rate in hydrocarbon reservoirs. In general, permeability increases with reservoir porosity. However, recent studies have shown that porosity is not a particularly reliable indicator of permeability and the effect of pore structure (pore aspect ratio and distribution) should be considered. In this study, four samples of tight sandstones were collected from the Q area of the Ordos Basin, China, including two samples with the same porosity but different permeabilities, and two samples with the same permeability but different porosities. X-ray-diffraction and thin-section analyses and experiments, under variable pressure for ultrasonic waves and permeability, were carried out. Based on rock-physics modelling, the volume fraction, aspect ratio, and radius of pores/cracks are inverted and estimated with the P- and S-wave velocities and permeability as constraints. The results show good agreement between model predictions and measurements. A comparative analysis indicates that the pore/crack density, the distribution of the aspect ratio, and the radius jointly affect the permeability.

Key words: tight sandstone, permeability, porosity, pore geometry, ultrasonic velocities.

1. Introduction

The importance of developing geophysical exploration techniques is to provide information on the presence of subsurface structures and fluids (e.g. oil and gas resources and geological CO_2 storage) (Neuman, 2005; Carcione *et al*., 2006; Jang and Santamarina, 2014; Tsang *et al*., 2015; Li *et al*., 2018; Qin *et al*., 2018; Zhou *et al*., 2019) and to indicate fluid mobility in the subsurface (Carman, 1956; Whitaker, 1986). To adequately estimate permeability, studies have been conducted on the relationships between rock physical properties/attributes and permeability (Gomez *et al*., 2010; Heidari and Li, 2014; Yu J. *et al*., 2014, 2020; Chen *et al*., 2017; Carcione *et al*., 2018, 2019, 2020; Santos *et al*., 2019; Madadi and Müller, 2021; Yu B. *et al*., 2022). Extensive experimental data show that there is no strong correlation between the other physical properties of rocks and permeability. The permeability of different rocks with similar physical properties can vary by several orders of magnitude (Brace, 1980), while the size of rock pores and the connectivity between pores can play a crucial role (Guéguen, 1994).

Considering that pore geometry can affect the elasticity and transport properties of rocks (Amalokwu and Falcon-Suarez, 2021; Zhang L. *et al*., 2021), its estimation has become an important research topic. The use of micro/nano-scale CT scans enables the direct observation of the three-dimensional pore structure of rocks at the nanometre to millimetre scale (Dong and Blunt, 2009). Xie *et al*. (2010) and Verwer *et al*. (2011) demonstrated that pore structure affects

porosity and permeability; Manda *et al.* (2013) indicated that the pore structure of moldic pores is more complex than that of etched pores. The image scan observation method enables the direct detection of microscopic pore structures, but is characterised by high cost and long inspection times (Zhang Y. and Toksöz, 2012). Therefore, the prediction of micropore structures based on rock-physical properties or attributes has attracted the attention of academic and industrial researchers.

Kuster and Toksöz (1974) proposed a model (K-T) which shows the effects of pore structures with different shapes on wave velocities. Subsequently, based on the K-T model, Cheng and Toksöz (1979) inverted the aspect ratio spectrum of various rocks as a function of pressure using the measured velocities, which could match the results of scanning electron microscopy. Tran *et al.* (2008) calculated the aspect ratio spectrum of Berea sandstone after heat treatment based on the differential effective medium (DEM) theory and discussed the relationships between that spectrum and temperature. Izumotani and Onozuka (2013) used the simulated annealing algorithm to predict the spectrum. Based on the Mori-Tanaka theory (Mori and Tanaka, 1973), David and Zimmerman (2012) inverted the spectrum of dry rocks, and Duan *et al.* (2018) explained the velocities in saturated rocks under variable confining pressures. To improve the accuracy of the inversion results, Tang *et al.* (2021) assigned different aspect ratios to each pore phase based on the elastic wave propagation theory proposed by Tang (2011) and compared them with the results of scanning electron microscopy.

To ensure the uniqueness of the inversion, previous studies have also attempted to estimate the aspect ratio spectrum together with several attributes. Based on the theory of Cheng and Toksöz (1979), Yan *et al.* (2014) took the porosities under different pressures as a constraint to improve the reliability of the inversion, and analysed the effects of fluid flow in the rock on wave dispersion and attenuation according to the model of Tang (2011). Due to the influence of pores on the estimated elastic moduli for the self-consistent (SC) model, Han *et al.* (2016) showed that the use of this model, with acoustic velocities and conductivity as constraints, did not lead to a spectrum that matched the experimental results. Based on the R-DEM model (Cilli and Chapman, 2021), Zhang L. *et al.* (2022) appropriately interpreted the measured nitrogen- and brine-saturated cases for P- and S-wave velocities, porosity, and conductivity and investigated the effects of conductivity on the spectrum. However, their work did not consider the pore radius.

After completing the construction of the rock pore structure, joint characterisation can be performed for permeability and the other physical rock properties (Kozeny, 1927; Doyen, 1988; Terzaghi *et al.*, 1996; Esteban *et al.*, 2007; Weger *et al.*, 2009; Geraud *et al.*, 2010; Grude *et al.*, 2015; Koestel *et al.*, 2018). Seeburger and Nur (1984) developed a two-dimensional network model that successfully explained the permeability of sandstone. Bernabé (1995) simulated the transport properties of Newtonian fluids in rocks using a network model consisting of pipes. Subsequently, Bernabé (2009) derived the hydraulic conductivity and wave propagation equations of rigid and elastic networks with saturating Newtonian fluids under periodic oscillations and calculated the hydraulic conductivity with different pipe lengths and radii in the network model. Johnson *et al.* (1987) conducted a study on dynamic permeability as a function of frequency. Blunt and King (1991) and Blunt (2001) constructed network models, analysed the migration of multiphase flows in centimetre-scale rock structures, and showed the relationship between permeability and saturation. Two-dimensional models have also been extended to three dimensions to explain the process of dewatering and water injection in sandstones (Nilsen *et al.*, 1996; Bakke and Øren, 1997). Xiong *et al.* (2020) used a three-dimensional pore structure model to analyse the rheological properties of fluids and the influences of pore cross connectivity on rock permeability, and proved that the frequency and connectivity between pores affect

permeability. These works have laid the foundation for further studies on the prediction of permeability in complex porous media.

To investigate the relationship between permeability and pore structure, four samples from tight-sandstone reservoirs in the Q area of the Ordos Basin were selected in this study. Thin section and X-ray diffraction (XRD) mineral analyses were performed, and rock physics experiments were carried out to measure ultrasonic velocities and permeabilities at different pressures. By simplifying the rock structure into pores and cracks, a differential effective medium model was used to describe the experimental data. This approach enables the estimation of the pore structure (aspect ratios, volume fractions and radius) and facilitates the analysis of other factors influencing permeability.

2. Samples and experimental procedures

2.1. Samples

In this study, the relationship between the pore/crack structure and the permeability for the four sandstone samples (identified as A, B, C, and D) is investigated. All samples were collected from the Chang-7 part of the Ordos Basin at a depth from 1,500 to 2,300 m below the surface. As shown in Fig. 1, all samples are relatively tight due to diagenetic variations, with feldspar
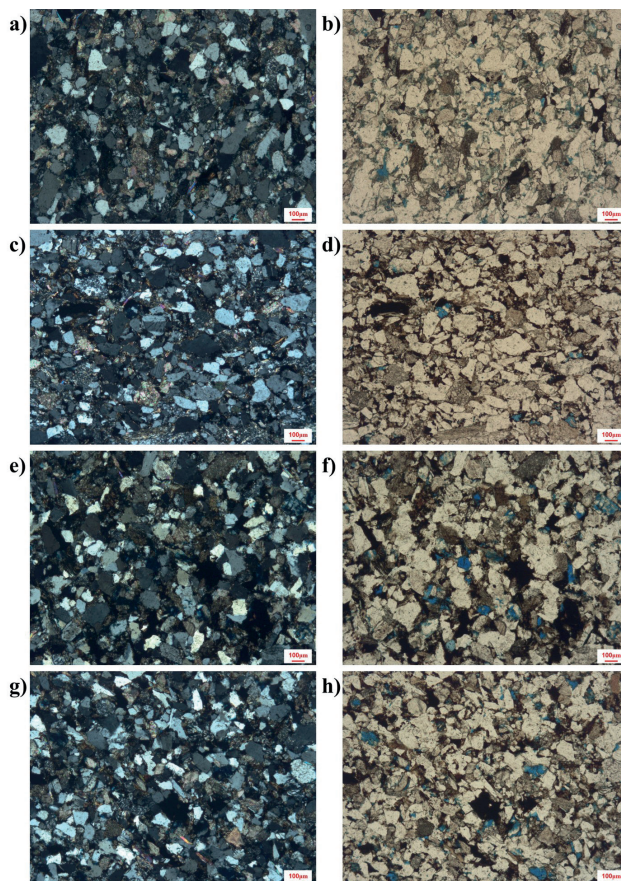

Fig. 1 - Thin section analyses of the tight sandstones: the orthogonal polarisation image (a) and single polarisation image (b) of sample A; the orthogonal polarisation image (c) and single polarisation image (d) of sample B; the orthogonal polarisation image (e) and single polarisation image (f) of sample C; the orthogonal polarisation image (g) and single polarisation image (h) of sample D. The blue areas in the single polarisation images represent the pores.

dissolution pores, mold pores, and residual intergranular pores. Pores and cracks of different sizes can be observed. The XRD analysis shows that the minerals in the four samples mainly consist of quartz, K-feldspar, plagioclase, and clay minerals. The specific contents of the constituents are listed in Table 1.

Table 1 - Mineral compositions of the samples.

samples	A	B	C	D
Quartz (%)	48.59	52.47	56.15	54.73
K-feldspar (%)	7.90	7.60	5.20	4.73
Plagioclase (%)	18.66	22.47	19.33	20.19
Calcite (%)	2.02	2.34	3.85	4.77
Ankerite (%)	6.96	2.77	-	-
Dolomite (%)	8.95	3.32	5.68	7.67
Siderite (%)	1.05	1.19	2.67	0.75
Clay (%)	5.87	7.84	7.12	7.16

2.2. Ultrasonic velocity measurement

The four samples are cut into cylindrical shapes. The ultrasonic tests are carried out using the same test setup as in Guo *et al*. (2009). The velocities are determined as follows:

$$V = \frac{L}{T_m - T_0} \tag{1}$$

where V stands for the P- and S-wave velocities, L for the sample length, T_m for the ultrasonic transit time, and T_0 for the system travel time.

At room temperature (~20 °C), nitrogen is used as a pore fluid for ultrasonic experiments. At the beginning, the confining pressure is set to 5 MPa, then, the pore pressure is increased to approximately 5 MPa and kept constant. To avoid an uneven distribution of pore pressure within the sample due to rapid confining pressure loading, the confining pressure loading rate is set to 0.1 MPa/min. The confining pressure is gradually increased to 60 MPa. When the confining pressure reaches 5, 10, 20, 30, 40, 50, and 60 MPa, the P and S waveforms are recorded. At each confining pressure, the condition of the sample is maintained for two hours to ensure pore pressure equilibrium. After data collection at all pressures, the confining pressure is gradually released.

2.3. Porosity and permeability measurements

The gas expansion method is used to determine the porosity of rock samples. Helium, which has a low molecular weight compared to nitrogen, can easily penetrate small pores. It is, therefore, used for porosity measurement due to the tight structure of the sample.

Permeability is measured using the pulse attenuation technique (Yang and Dong, 2017), with corrections made for the Klinkenberg slippage effect (Klinkenberg, 1941). At room temperature (~20 °C), the pore pressure is kept at 0 MPa, while the confining pressure is set to 5, 15, 25, 35, and 45 MPa to measure the permeability.

3. Rock-physics models

3.1. The DEM model

The DEM model considers the isotropic mineral grains as the host phase (matrix) and the pore fluid as inclusions. In each calculation, the inclusion with a lower volume fraction is placed within the host phase, and the host phase and inclusions are combined to calculate the effective elastic moduli of the composite material. At this point, it is assumed that the host phase with the inclusion is uniformly isotropic, and a new host phase is calculated. Other inclusions of different sizes and shapes are, then, added to this new host phase for further computation. This process is iterated multiple times until the content of each component in the material reaches the desired values.

The equations for the multiphase DEM model are derived according to Berryman (1992):

$$(1-c)\frac{\mathrm{d}K^*}{\mathrm{d}c}=\left(K_2-K^*\right)P^{(*i)} \tag{2a}$$

$$(1-c)\frac{\mathrm{d}\mu^*}{\mathrm{d}c}=\left(\mu_2-\mu^*\right)Q^{(*i)}. \tag{2b}$$

In the first iteration, K^* and μ^* represent the bulk and shear moduli of the host, respectively. K_2, μ_2, and c are the bulk modulus, shear modulus, and volume fraction of the inclusion, and K^* and μ^* are the effective bulk and shear moduli, respectively. $P^{(*i)}$ and $Q^{(*i)}$ are the geometric factors of inclusion.

3.2. Pressure dependence

The elastic modulus related to pressure enables the extraction of distribution characteristics related to rock pore structure, such as aspect ratio, crack density, crack porosity, and crack radius (Toksöz et al., 1976; Tran et al., 2008; David and Zimmerman, 2012). The method proposed by Toksöz et al. (1976) has demonstrated applicability across diverse rock types exhibiting different porosities, thus, facilitating predictions of elastic wave velocities under varying fluid saturations within the rock.

To predict the pore/crack structure at different effective pressures, P_d, the closure of pores and cracks must be determined. Toksöz et al. (1976) provided the equation for the variation of the coin-shaped pore/crack volume fraction, c, at different pressures as:

$$\frac{dc(\alpha)}{c(\alpha)}=-\frac{P_d/K_A^*}{E_1-\dfrac{E_2E_3}{E_3+E_4}} \tag{3}$$

where α is the aspect ratio, K_A^* is the dry-rock bulk modulus. E_m ($m = 1, 2, 3, 4$) denotes the functions relating to the aspect ratio and effective bulk and shear moduli at different effective pressures, i.e.:

$$E_1 = 3\mu I_a / \pi (3K + 4\mu) \tag{4a}$$

$$E_2 = 3\mu / (2\pi (3K + 4\mu))(3I_a - 4\pi) \tag{4b}$$

$$E_3 = \alpha^2 \left[3 - (9I_a / 4\pi) \right] [3K + \mu] / \left((1 - \alpha^2)(3K + 4\mu) \right) \\ + 3\mu I_a / (4\pi (3K + 4\mu)) \tag{4c}$$

$$E_4 = \left[3 - (9I_a / 4\pi) \right] [3K + \mu] / \left(2(1 - \alpha^2)(3K + 4\mu) \right) \\ - 3\mu (1 - I_a / \pi) / (3K + 4\mu) \tag{4d}$$

$$I_a = \frac{2\pi\alpha}{(1 - \alpha^2)^{3/2}} \left(\cos^{-1}\alpha - \alpha (1 - \alpha^2)^{1/2} \right). \tag{4e}$$

The change rate of the aspect ratio of a coin-shaped pore with pressure is equal to the change rate of the volume fraction (Cheng and Toksöz, 1979). Therefore, the volume fraction and aspect ratio of each inclusion at the *l*-th effective pressure are:

$$c_{lk} = c_{0k} \left(1 + \frac{dc}{c} (\alpha_{0k}, P_{d,l}) \right) \tag{5a}$$

$$\alpha_{lk} = \alpha_{0k} \left(1 + \frac{dc}{c} (\alpha_{0k}, P_{d,l}) \right) \tag{5b}$$

where c_{0k} and α_{0k} are the values at zero effective pressure. When $d\alpha/\alpha \leq -1$, the pressure is considered to be very high and the cracks close, so that the corresponding volume fraction of inclusions is zero. Eqs. (3) to (5) can be used to calculate the change in the pore and crack structure at different effective pressures.

3.3. Inversion algorithm

1. The grain bulk and shear moduli are obtained with the Voigt-Reuss-Hill (VRH) method proposed by Voigt (1928), Reuss (1929) and Hill (1952), i.e.:

$$M_V = \sum_{i=1}^{N} f_i M_i \tag{6a}$$

$$\frac{1}{M_R} = \sum_{i=1}^{N} \frac{f_i}{M_i} \tag{6b}$$

$$M_{VRH} = \frac{M_V + M_R}{2} \tag{6c}$$

where N is the number of mineral components, f_i is the volume fraction corresponding to the i-th mineral component determined by XRD mineral analysis, M_i denotes the elastic moduli of the mineral, and M_V and M_R are the upper and lower bounds of the grain moduli, respectively. M_{VRH} denotes the effective elastic moduli.

2. The pore aspect ratio is the unknown property required to compute V_P and V_S by the DEM model (Mavko et al., 2009). A series of assumed volume fractions and aspect ratios of pores/cracks are attributed to the rock matrix. The aspect ratios of pores and cracks are typically between 0.01 and 1 for pores, and between 0.000001 and 0.01 for cracks. Following the methodology proposed by Izumotani and Onozuka (2013), the aspect ratios of cracks are distributed logarithmically, while the volume fraction of each crack is random. The sum of the volume fractions of pores and cracks equals the measured porosity. Next, the effective elastic moduli are obtained.

3. The effective bulk modulus, K^*, and shear modulus, μ^*, are calculated as a function of pressure and the predicted P- and S-wave velocities are obtained as $V_{Pl}^{\text{Predict}} = \sqrt{\left(K^* + 4/3\mu^*\right)/\rho}$ and $V_{Sl}^{\text{Predict}} = \sqrt{\mu^*/\rho}$.

4. The interior point method proposed by Adler et al. (1989) is used to find the optimal solution for the pore/crack structure. The objective function to be minimised is the sum of the squared errors between the theoretical predictions and the experimental data, namely:

$$F_{ela}\left(\alpha_{01}, \alpha_{02}, \ldots \alpha_{0n}, c_{01}, c_{02}, \ldots c_{0n}, K_g, \mu_g\right)$$
$$= \min\left[\sum_{l=1}^{L}\left(V_{Pl}^{\text{m}} - V_{Pl}^{\text{Predict}}\right)^2 + \sum_{l=1}^{L}\left(V_{Sl}^{\text{m}} - V_{Sl}^{\text{Predict}}\right)^2\right]$$

(7)

where α_{01}, α_{02}, ... α_{0n} and c_{01}, c_{02}, ... c_{0n} denote the aspect ratio and the volume fraction, respectively. L is the number of pressures, and V_{Pi}^{m} and V_{Si}^{m} are the measured P- and S-wave velocities. Building upon relevant theories, a modelling approach is proposed, and depicted in Fig. 2.

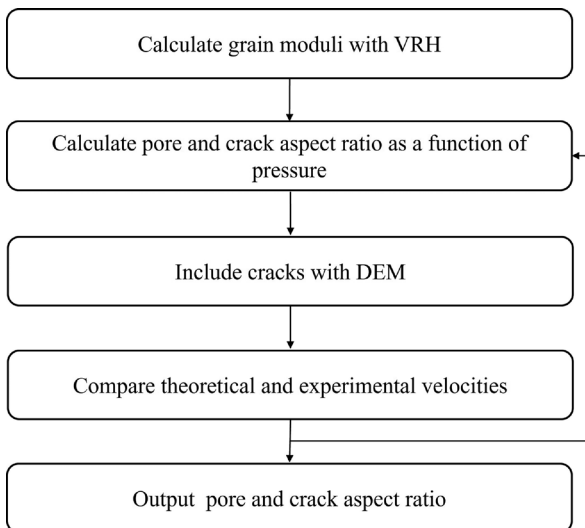Fig. 2 - Modelling and inversion flowchart.

4. Relation between permeability and pore structure

4.1. Aspect ratio of pores/cracks and volume fraction

Figs. 3 and 4 show the experimental data of V_P and V_S at a confining pressure of 5-60 MPa under nitrogen-saturated conditions and the inverted aspect ratio spectra for samples A, B, C, and D, respectively. The closure of pores and cracks with pressure leads to an increase in bulk and shear moduli (Yin *et al.*, 2017), resulting in an increase in the velocities. The density, bulk modulus, and viscosity of nitrogen are 112.6 kg/m³, 0.0161 GPa, and 0.000017 Pa·s, respectively. The inversion grain bulk/shear moduli for samples A, B, C, and D are 45 GPa/35 GPa, 48 GPa/32 GPa, 43 GPa/34 GPa, and 37 GPa/36 GPa, respectively, and R² for the velocities are 0.9503 and 0.8878, 0.9945 and 0.9880, 0.982 and 0.9718, and 0.9628 and 0.8199, respectively, indicating that the model can adequately explain these measurements.

In Figs. 3b and 4b, the first two histograms correspond to pores and the others to cracks. For sample A, the aspect ratio and the volume fraction of the two pores are 0.05 and 5×10⁻⁵, and 0.3 and 0.0695. The crack volume fraction is highest when the aspect ratio is 0.0015. For sample B, these values are 0.1 and 0.0061, and 0.4 and 0.0477. The cracks with an aspect ratio of 0.0063 have the highest volume fraction. The aspect ratio distribution for sample A and B is between 6.31×10⁻⁵ and 0.0063, but for sample B, the cracks with an aspect ratio between 0.0032 and 0.0063 and between 6.3×10⁻⁵ and 1.26×10⁻⁴ have higher volume fractions. For sample C, the pore aspect ratios are 0.3 and 0.04, with the highest volume fraction observed for cracks with an aspect ratio of 0.0032. Similarly, the pore aspect ratios for sample D are 0.03 and 0.3, with the highest volume fraction for cracks with an aspect ratio of 0.0032. The distribution of crack aspect ratios for samples C and D ranges from 3.162×10⁻⁵ to 0.0032. In each sample, the higher the aspect ratio, the higher the pore volume fraction. Although the pore- or crack-filling fluid is added to the host phase in the same way, resulting in similar aspect ratio distributions, the pore or crack volume fraction can be quite different between samples.

Table 2 shows that samples A and B have the same permeability, with the porosity of B being lower than that of A. Samples C and D have similar porosities, while sample D has a higher permeability. As shown in Figs. 3b and 4b, samples B and D have higher volume fractions of low aspect ratio cracks. Cracks provide a relatively direct path for the fluid to flow more easily. The
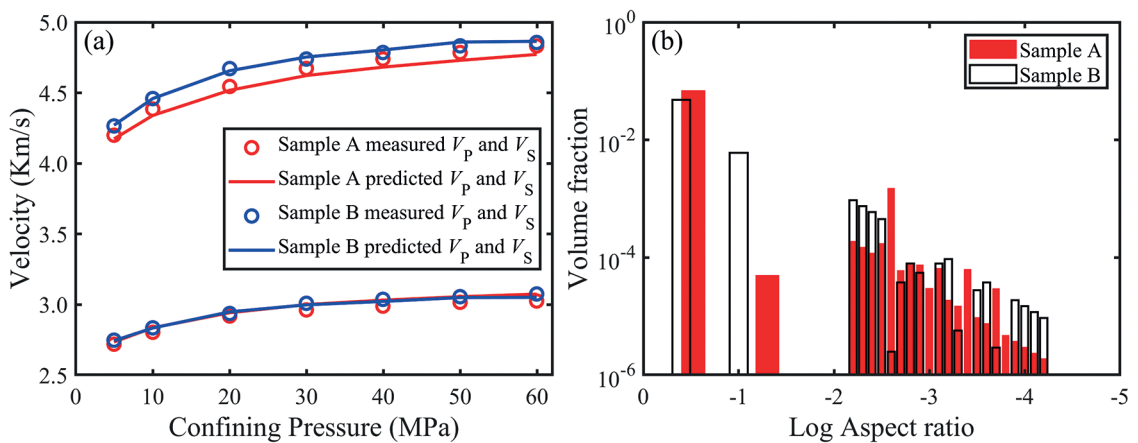

Fig. 3 - Comparison between the measured and theoretical velocities as a function of differential pressure for samples A and B (a), and the estimated pore-aspect-ratio spectra (b).

presence of cracks also increases the surface area of the rock available for fluid flow within the rock. This leads to an increase in permeability. In addition, cracks with a low aspect ratio tend to form continuous and interconnected channels. In contrast, cracks with a higher aspect ratio may be more circular or spherical, and the flow may be obstructed by crack edges and corners.
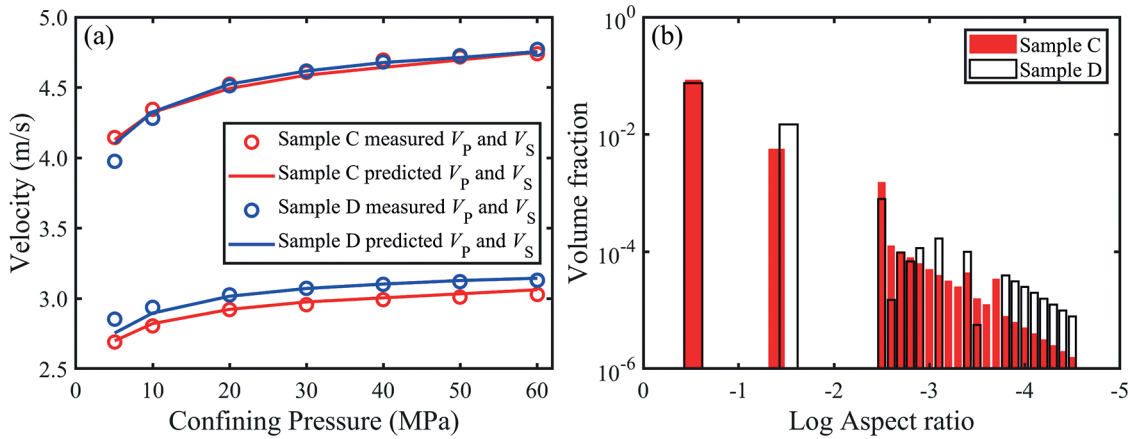

Fig. 4 - Comparison between the measured and theoretical velocities as a function of differential pressure for samples C and D (a), and the estimated pore-aspect-ratio spectra (b).

Table 2 - Physical properties of the samples.

Sample	A	B	C	D
Density (g/cm³)	2.49	2.51	2.44	2.41
Porosity (%)	7.220	5.787	9.201	9.222
Permeability (mD)	0.020	0.020	0.038	0.066

4.2. Crack density

The crack density can be obtained as (Kachanov, 1993):

$$\rho_c = \frac{\phi_c}{2\pi\alpha} \tag{8}$$

where ϕ_c is the crack porosity.

Figs. 5a and 5b show the distribution of crack density for samples A, B, C, and D, ranging from 0.0048 to 0.0955, 0.0018 to 0.0239, 0.0080 to 0.0768, and 9.5763×10^{-4} to 0.0398, respectively. The overall crack densities are 0.25, 0.29, 0.265, and 0.465, respectively. Sample B has a lower porosity, but its overall crack density is higher, indicating better interconnection of the cracks within the skeleton. Although sample C and D have the same porosity, the total crack density of sample D is much higher than that of C, resulting in a higher permeability. As the crack density increases, the distance between cracks decreases, consequently increasing connectivity (Xiong et al., 2021). The connectivity of cracks plays an important role in permeability.

Similar characteristics observed in the two groups are as follows. In specimens A and C, cracks

with a high aspect ratio have a higher crack density. In samples B and D, on the other hand, the distribution of crack density with respect to aspect ratio is more uniform, and the crack densities, corresponding to small aspect ratios, have higher proportions.
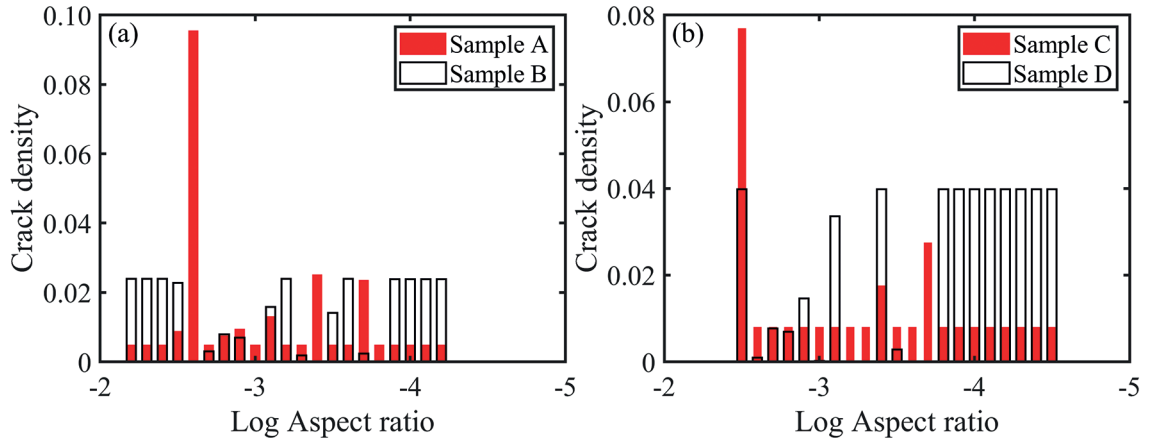

Fig. 5 - Crack density as a function of the aspect ratio of samples A and B (a), and of samples C and D (b).

4.3. Prediction of pore and crack radii

The geometric shapes of pores/cracks can be used to predict rock permeability. The total permeability, κ, of the rock is assumed to be composed of matrix permeability, κ_p, and crack permeability, κ_c, and that both pores and cracks consist of cylindrical bodies with radius r:

$$\kappa(P_d) = \kappa_p(P_d) + \kappa_c(P_d). \tag{9}$$

Based on the work by Al-Wardy and Zimmerman (2004), matrix permeability κ_p can be derived as:

$$\kappa_p = \frac{c_k r_k^2}{8} \tag{10}$$

where c_k and r_k are the volume fraction and radius of the pores, respectively.
From Sarout (2012), crack permeability κ_c is:

$$\kappa_c : \frac{16}{27} \frac{c_m r_m^2 \alpha_m^2 \left(1 - \alpha_m^2\right)}{\left(2\sqrt{1-\alpha_m^2} + \alpha_m^2 \log\left(\frac{2 - \alpha_m^2 + 2\sqrt{1-\alpha_m^2}}{\alpha_m^2}\right)\right)^2} \tag{11}$$

where c_m, r_k, and α_m are the volume fraction, radius and aspect ratio of the cracks.
Based on the incremental algorithm, the equivalent permeability model is applied to the case of multiple components by using the aspect ratio spectrum as input. The matrix permeability

and crack permeability are calculated using Eqs. (10) and (11), respectively.

The mean-square error between the theoretical predictions and the experimental permeability values is considered as the objective function for estimating the radius, i.e.:

$$F_{ela}(r_{01}, r_{02}, \ldots, r_{0k}) = min\left[\sum_{n=1}^{N}\left(\kappa_{p,n} - \kappa_{p,n}^{Pre}\right)^2 + \sum_{n=1}^{N}\left(\kappa_{c,n} - \kappa_{c,n}^{Pre}\right)^2\right] \qquad (12)$$

The relation between permeability and confining pressure can be represented by a combination of linear and exponential terms (Shapiro, 2003; Shapiro et $al.$, 2015). The results are:

sample A, $\kappa = 5.56\times10^{-4} - 5.25\times10^{-6}\,P + 0.0051e^{-0.0977P}$ (R^2 = 0.9926)

sample B, $\kappa = 7.013\times10^{-4} - 4.2714\times10^{-6}\,P + 0.0014e^{-0.1056P}$ (R^2 = 0.9982)

sample C, $\kappa = 0.0012 - 1.264\times10^{-5}\,P + 0.016e^{-0.1002P}$ (R^2 = 0.9999)

sample D, $\kappa = 0.017 - 10^{-4}\,P + 0.0364e^{-0.1344P}$ (R^2 = 0.9997).

In each empirical relation, the first two terms represent the matrix permeability and the last the crack permeability.

Figs. 6 to 9 show the aspect ratio and volume fractions of pores and cracks at different confining pressures. Pores with an aspect ratio from 0.019 to 1 are stiff, and, in such case, the volume fraction and aspect ratio do not significantly change with pressure. Cracks with smaller aspect ratios tend to close with increasing pressure, while the volume fraction and aspect ratio of cracks with larger aspect ratios gradually decrease. As the pressure increases, the stiffness of the rock increases and the closing rate of the cracks gradually decreases as a function of pressure. According to Eqs. (3) to (5), crack closure occurs when $dc(\alpha)/c(\alpha)$ is less than -1. Cracks with aspect ratios below 10^{-4} close when the confining pressure reaches 20 MPa. As the confining pressure increases to 60 MPa, cracks with aspect ratios between 10^{-3} and 10^{-2} do not
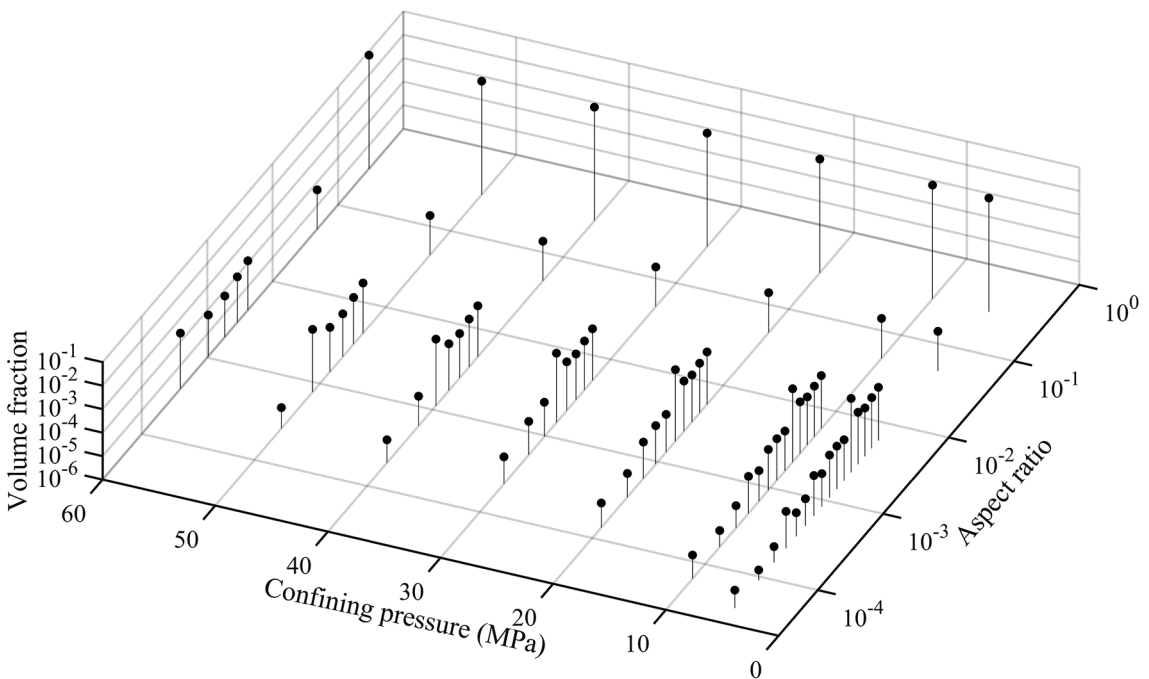

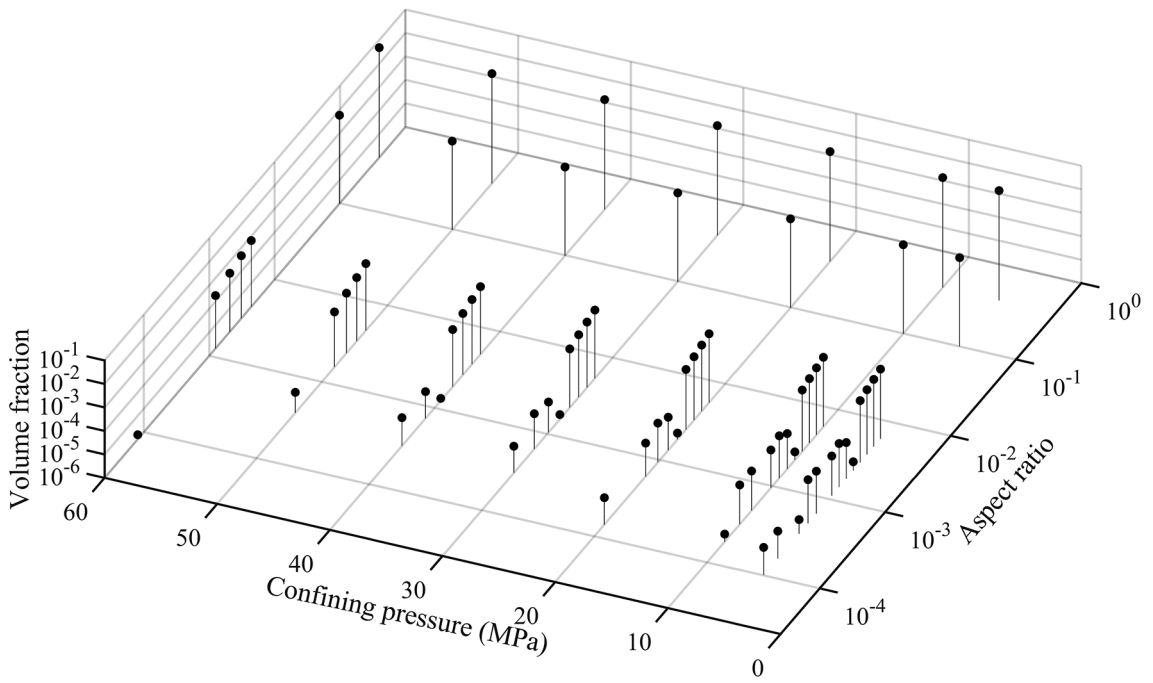Fig. 6 - Spectrum of the pore and crack aspect ratio of sample A at different pressures.

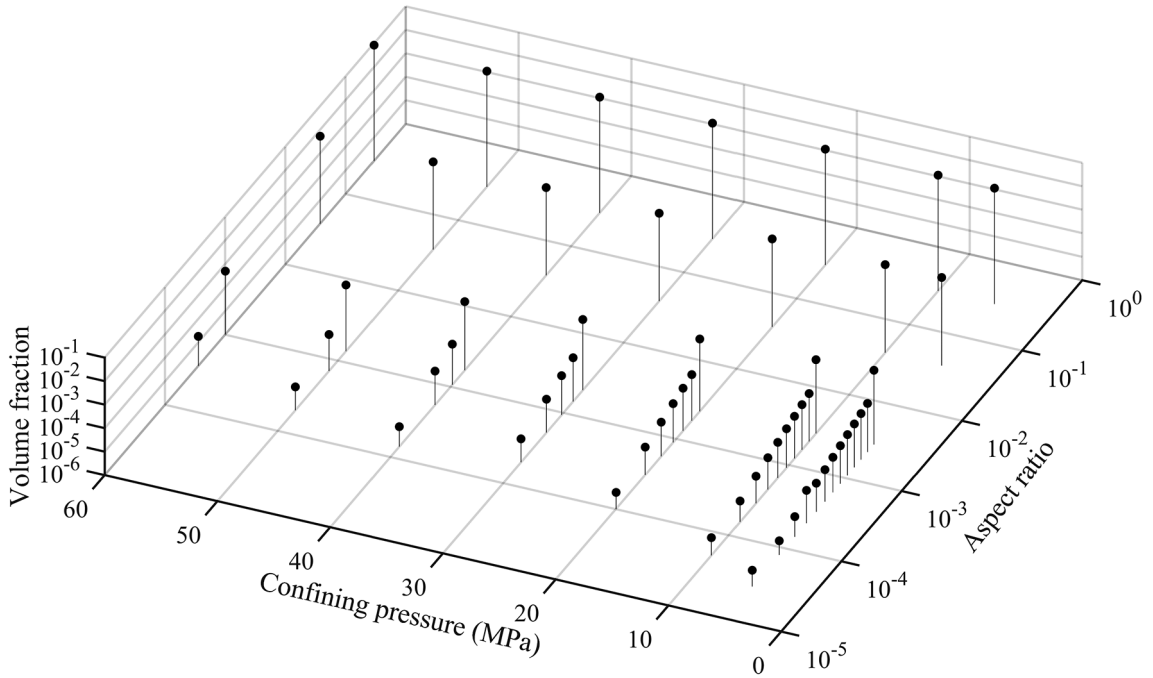Fig. 7 - Spectrum of the pore and crack aspect ratio of sample B at different pressures.

Fig. 8. Spectrum of the pore and crack aspect ratio of sample C at different pressures.

close completely, but their aspect ratios gradually decrease. Notably, cracks with smaller aspect ratios require lower closure stresses.
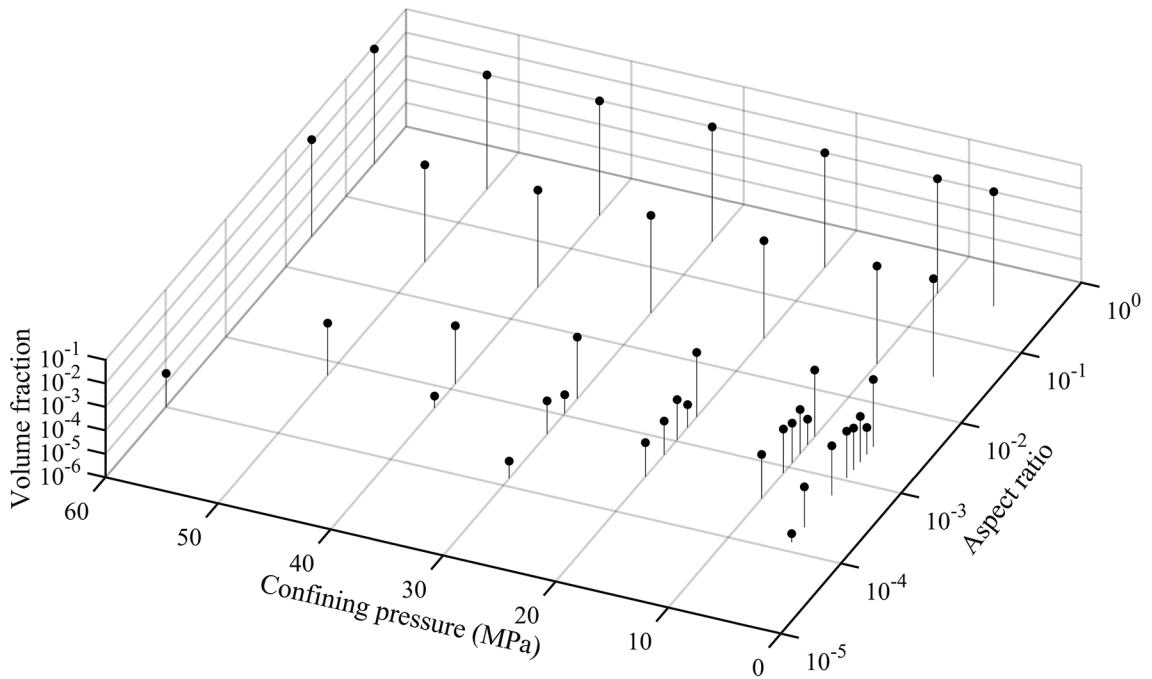
Fig. 9 - Spectrum of the pore and crack aspect ratio of sample D at different pressures.

Figs. 10 and 11 show the comparison between the measured permeability and the predicted values as well as the predicted pore/crack radius spectra. The R^2 of samples A, B, C, and D are 0.9922, 0.9477, 0.9938, and 0.9527, respectively. A comparison of the pore and crack radii shows that the majority of the crack radii are larger than the pore radii. Xiong *et al*. (2020) proved that the larger radii facilitate the formation of migration pathways for fluid flow, resulting in increased permeability. Davudov and Moghanloo (2018) proved that, with increasing pressure, the connectivity between pores/cracks decreases, leading to a decrease in permeability.
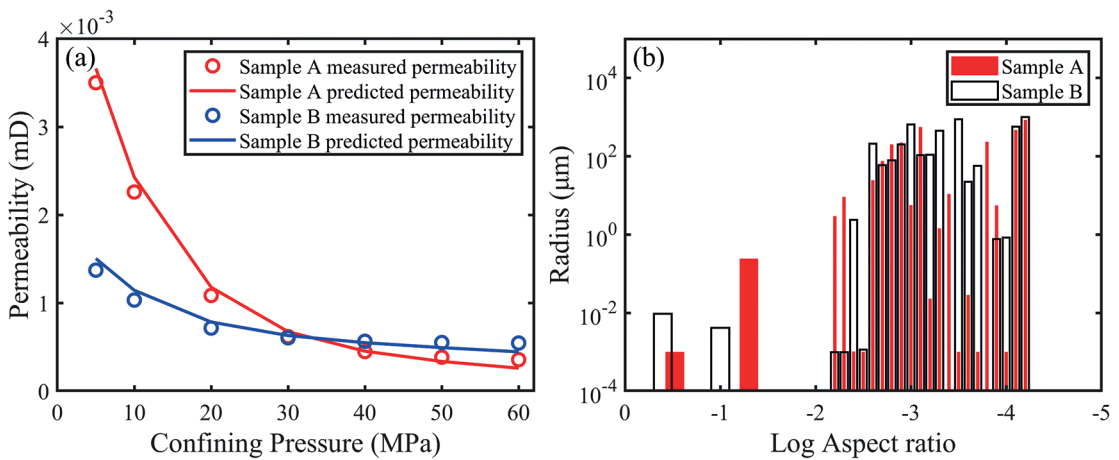

Fig. 10 - Permeability as a function of confining pressure, predicted and measured (a), and estimated pore and crack spectra for samples A and B (b).
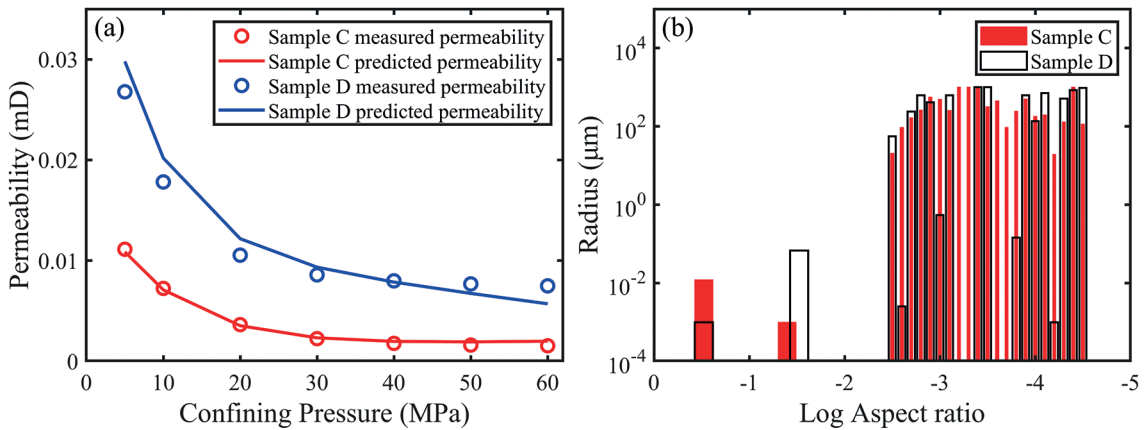
Fig. 11 - Permeability as a function of confining pressure, predicted and measured (a), and estimated pore and crack spectra for samples C and D (b).

5. Conclusions

In this study, XRD analysis, thin section analysis, permeability, and ultrasonic experiments are performed on four samples of tight sandstones from the Yanchang Formation of the Ordos Basin. Based on the DEM theory, a rock-physics model for the inversion of pore structure is established, and proof is given that the estimation effectively explains the experimental data.

The results show that when fluids flow through small aspect ratio cracks, the short distance travelled results in low resistance, which increases permeability. The higher crack density and the smaller distances between pores and cracks improve the internal connectivity of the rock, thus, increasing permeability. When a confining pressure is applied to the rock, cracks with larger radii and smaller aspect ratios close first, reducing the connectivity of the pore system and leading to a sharp decrease in permeability. If the pressure is increased further, the pore structure of the rock is more stable during deformation, which leads to a gradual weakening of the reduction in permeability.

In this study, the objective function mainly focuses on the elastic parameters. The conductivity effect could be integrated into the objective function in the future, potentially improving the accuracy of the results. It would also be valuable to explore the effects of pore connectivity in future studies.

REFERENCES

Adler I., Resende M., Veiga G. and Karmarkar N.; 1989: *An implementation of Karmarkar's algorithm for linear programming.* Math. Programm., 44, 297–335, doi: 10.1007/BF01587095.

Al-Wardy W. and Zimmerman W.; 2004: *Effective stress law for the permeability of clay-rich sandstones*. J. Geophys. Res. B: Solid Earth, 109, 6 pp., doi: 10.1029/2003JB002836.

Amalokwu K. and Falcon-Suarez I.; 2021: *Effective medium modeling of pressure effects on the joint elastic and electrical properties of sandstones*. Journal of Petroleum Science and Engineering, 202, 10 pp., doi: 10.1016/j.petrol.2021.108540.

Bakke S. and Øren P.; 1997: *3-D pore-scale modelling of sandstones and flow simulations in the pore networks*. SPE Journal, 2, 136-149, doi: 10.2118/35479-PA.

Bernabé Y.; 1995: *The transport properties of networks of cracks and pores*. J. Geophys. Res. B: Solid Earth, 100, 4231–4241, doi: 10.1029/94JB02986.

Bernabé Y.; 2009: *Oscillating flow of a compressible fluid through deformable pipes and pipe networks: wave propagation phenomena*. Pure Appl. Geophys., 166, 969–994, doi: 10.1007/s00024-009-0484-3.

Berryman G.; 1992: *Single-scattering approximations for coefficients in Biot's equations of poroelasticity*. J. Acoust. Soc. Am., 91, 551–571, doi: 10.1121/1.402518.

Blunt M.; 2001: *Flow in porous media—pore-network models and multiphase flow*. Curr. Opin. Colloid Interface Sci., 6, 197-207, doi: 10.1016/S1359-0294(01)00084-X.

Blunt M. and King P.; 1991: *Relative permeabilities from two- and three-dimensional pore-scale network modelling*. Transport in Porous Media, 6, 407-433, doi: 10.1007/BF00136349.

Brace W.; 1980: *Permeability of crystalline and argillaceous rocks*. Int. J. Rock Mech. Min. Sci Geomech. Abstr., 17, 241–251, doi: 10.1016/0148-9062(80)90807-4.

Carcione J.M., Picotti S., Gei D. and Rossi G.; 2006: *Physics and seismic modeling for monitoring CO_2 storage*. Pure Appl. Geophys., 163, 175-207, doi: 10.1007/s00024-005-0002-1.

Carcione J.M., Poletto F., Farina B. and Bellezza C.; 2018: *3D seismic modeling in geothermal reservoirs with a distribution of steam patch sizes, permeabilities and saturations, including ductility of the rock frame*. Phys. Earth Planet. Interiors, 279, 67-78, doi: 10.1016/j.pepi.2018.03.004.

Carcione J.M., Gei D., Yu T. and Ba J.; 2019: *Effect of clay and mineralogy on permeability*. Pure Appl. Geophys., 176, 2581-2594, doi: 10.1007/s00024-019-02117-3.

Carcione J.M., Gei D., Picotti S., Misnan M.S., Rashidi M.R.A., Bakar Z.A.A., Harith Z.Z.T., Bahri N.H.S. and Hashim N.; 2020: *Porosity and permeability of the overburden from wireline logs: a case study from offshore Malaysia*. Geomech. Geophys. Geo-energ. Geo-resour., 6, 12 pp., doi:10.1007/s40948-020-00172-y.

Carman P.; 1956: *Flow of gases through porous media*. Academic Press, New York, NY, USA, 182 pp.

Chen X., Yu J., Tang C., Li H. and Wang S.; 2017: *Experimental and numerical investigation of permeability evolution with damage of sandstone under triaxial compression*. Rock Mech. Rock Eng., 50, 1529-1549, doi: 10.1007/s00603-017-1169-3.

Cheng C. and Toksöz M.; 1979: *Inversion of seismic velocities for the pore aspect ratio spectrum of a rock*. J. Geophys. Res.: Solid Earth, 84, 7533-7543, doi: 10.1029/JB084iB13p07533.

Cilli P. and Chapman M.; 2021: *Linking elastic and electrical properties of rocks using cross-property DEM*. Geophys. J. Int., 225, 1812-1823, doi: 10.1093/gji/ggab046.

David E. and Zimmerman R.; 2012: *Pore structure model for elastic wave velocities in fluid-saturated sandstones*. J. Geophys. Res.: Solid Earth, 117, 15 pp., doi: 10.1029/2012JB009195.

Davudov D. and Moghanloo R.; 2018: *Impact of pore compressibility and connectivity loss on shale permeability*. Int. J. Coal Geol., 187, 98-113, doi: 10.1016/j.coal.2018.01.008.

Dong H. and Blunt M.; 2009: *Pore-network extraction from micro-computerised-tomography images*. Phys. Rev. E: Stat. Nonlinear Soft Matter Phys., 80, doi: 10.1103/PhysRevE.80.036307.

Doyen P.; 1988: *Permeability, conductivity, and pore geometry of sandstone*. J. Geophys. Res. Solid Earth, 93, 7729–7740, doi: 10.1029/JB093iB07p07729.

Duan C., Deng J., Li Y., Lu Y., Tang Z. and Wang X.; 2018: *Effect of pore structure on the dispersion and attenuation of fluid-saturated tight sandstone*. J. Geophys. Eng., 15, 449-460, doi: 10.1088/1742-2140/aa8b82.

Esteban L., Geraud Y. and Bouchez J.; 2007: *Pore network connectivity anisotropy in Jurassic argillite specimens from eastern Paris Basin (France)*. Phys. Chem. Earth, 32, 161-169, doi: 10.1016/j.pce.2005.11.001.

Geraud Y., Rosener M., Surma F., Place J., Garzic É. and Diraison M.; 2010: *Physical properties of fault zones within a granite body: example of the Soultz-sous-Forets geothermal site*. Comptes Rendus Géoscience, 342, 566–574, doi: 10.1016/j.crte.2010.02.002.

Gomez C., Dvorkin J. and Vanorio T.; 2010: *Laboratory measurements of porosity, permeability, resistivity, and velocity on Fontainebleau sandstones*. Geophysics, 75, 191–204, doi: 10.1190/1.3493633.

Grude S., Dvorkin J. and Landrø M.; 2015: *Permeability variation with porosity, pore space geometry, and cement type: a case history from the Snøhvit field, the Barents Sea*. Geophysics, 80, 43–49, doi: 10.1190/geo2014-0064.1.

Guéguen Y. and Palciauskas V.; 1994: *Introduction to the physics of rocks*. Princeton University Press, Princeton, NJ, USA, 294 pp.

Guo M.Q., Fu L.Y. and Ba J.; 2009: *Comparison of stress-associated coda attenuation and intrinsic attenuation from ultrasonic measurements*. Geophys. J. Int., 178, 447-456., doi: 10.1111/j.1365-246X.2009.04159.x.

Han T., Clennell M., Cheng A. and Pervukhina M.; 2016: *Are self-consistent models capable of jointly modeling elastic velocity and electrical conductivity of reservoir sandstones?*. Geophysics, 81, 377-382, doi: 10.1190/geo2015-0690.1.

Heidari P. and Li L.; 2014: *Solute transport in low-heterogeneity sandboxes: the role of correlation length and permeability variance*. Water Resour. Res., 50, 8240–8264, doi: 10.1002/2013WR014654.

Hill R.; 1952: *The elastic behaviour of a crystalline aggregate*. Proc. Phys.Soc., 6, 349-354, doi: 10.1088/0370-1298/65/5/307.

Izumotani S. and Onozuka S.; 2013: *Elastic moduli and the aspect ratio spectrum of rock using simulated annealing*. Geophys. Prospect., 61, 489-504, doi: 10.1111/1365-2478.12003.

Jang J. and Santamarina J.; 2014: *Evolution of gas saturation and relative permeability during gas production from hydrate-bearing sediments: gas invasion vs. gas nucleation*. J. Geophys. Res.: Solid Earth, 119, 116–126, doi: 10.1002/2013JB010480.

Johnson D.L., Koplik J. and Dashen R.; 1987: *Theory of dynamic permeability and tortuosity in fluid-saturated porous media*. J. Fluid Mech., 176, 379–402, doi: 10.1017/S0022112087000727.

Kachanov M.; 1993: *Elastic solids with many cracks and related problems*. Advances in Applied Mechanics, 30, 259-445, doi: 10.1016/S0065-2156(08)70176-5.

Klinkenberg L.J.; 1941: *The permeability of porous media to liquids and gases*. Drilling and Production Practice, API-41-200, 200–213, doi: 10.5510/OGP20120200114.

Koestel J., Dathe A., Skaggs T., Klakegg O., Ahmad M., Babko M., Gimenez D., Farkas C., Nemes A. and Jarvis N.; 2018: *Estimating the permeability of naturally structured soil from percolation theory and pore space characteristics imaged by X-ray*. Water Resour. Res., 54(, 9255–9263, doi: 10.1029/2018WR023609.

Kozeny J.; 1927: *Uber kapillare Leitung der wassers in Boden*. Sitzungsber Akad. Wiss., Wien, Austria, 136, 271-306.

Kuster G.T. and Toksöz M.; 1974: *Velocity and attenuation of seismic waves in two-phase media — Part 1: Theoretical formulations*. Geophysics, 39, 587–606, doi: 10.1190/1.1440450.

Li S., Qiao C., Li Z. and Hui Y.; 2018: *The effect of permeability on supercritical CO_2 diffusion coefficient and determination of diffusive tortuosity of porous media under reservoir conditions*. Journal of CO_2 Utilization, 28, 1–14, doi: 10.1016/j.jcou.2018.09.007.

Madadi M. and Muller T.; 2021: *Effect of porosity gradient on the permeability tensor*. Geophys. Prospect., 69, 542–551, doi: 10.1111/1365-2478.12922.

Manda A. and Culpepper A.; 2013: *Characterizing moldic and vuggy pore space in karst aquifers using borehole-wall slabbed-core and thin-section images*. J. Appl. Geophys., 88, 12-22, doi: 10.1016/j.jappgeo.2012.10.005.

Mavko G., Mukerji T. and Dvorkin J.; 2009: *The rock physics handbook*. Cambridge University Press, Cambridge , UK, 524 pp., doi: 10.1017/CBO9780511626753.

Mori T. and Tanaka K.; 1973: *Average stress in matrix and average elastic energy of materials with misfitting inclusions*. Acta Metall., 21, 571–574, doi: 10.1016/0001-6160(73)90064-3.

Neuman S.; 2005: *Trends, prospects and challenges in quantifying flow and transport through fractured rocks*. Hydrogeol. J., 13, 124-147, doi: 10.1007/s10040-004-0397-2.

Nilsen L., Øren P., Bakke S. and Henriquez A.; 1996: *Prediction of relative permeability and capillary pressure from a pore model*. In: European 3-D Reservoir Modelling Conference, Stavanger, Norway, paper no. SPE-35531-MS, doi: 10.2118/35531-MS.

Qin Y., Wu Y., Liu P., Zhao F. and Yuan Z.; 2018: *Experimental studies on effects of temperature on oil and water relative permeability in heavy-oil reservoirs*. Sci. Rep., 8, 9 pp., doi: 10.1038/s41598-018-31044-x.

Reuss A.; 1929: *Calculation of the flow limits of mixed crystals on the basis of the plasticity of monocrystals*. Z. Ang. Math., 9, 49-58, doi: 10.1002/zamm.19290090104.

Santos J.E., Savioli G.B., Carcione J.M. and Ba J.; 2019: *Effect of capillarity and relative permeability on Q anisotropy of hydrocarbon source rocks*. Geophys. J. Int., 218, 1199-1209, doi: 10.1093/gji/ggz217.

Sarout J.; 2012: *Impact of pore space topology on permeability, cut-off frequencies and validity of wave propagation theories*. Geophys. J. Int., 189, 481-492, doi: 10.1111/j.1365-246X.2011.05329.x.

Seeburger D. and Nur A.; 1984: *A pore space model for rock permeability and bulk modulus*. J. Geophys. Res.: Solid Earth, 89, 527–536, doi: 10.1029/JB089iB01p00527.

Shapiro S.; 2003: *Elastic piezosensitivity of porous and fractured rocks*. Geophysics, 68, 482–486, doi: 10.1190/1.1567215.

Shapiro S., Khizhniak G., Plotnikov V., Niemann R., Ilyushin P. and Galkin S.; 2015: *Permeability dependency on stiff and compliant porosities: a model and some experimental examples*. J. Geophys. Eng., 12, 376–385, doi: 10.1088/1742-2132/12/3/376.

Tang X.M.; 2011: *A unified theory for elastic wave propagation through porous media containing cracks — An extension of Biot's poroelastic wave theory*. Science China Earth Sciences, 54, 1441-1452, doi: 10.1007/s11430-011-4245-7.

Tang X.M., Wang H., Su Y. and Chen X.; 2021: *Inversion for micro-pore structure distribution characteristics using cracked porous medium elastic wave theory*. Chin. J. Geophys., 64, 2941-2951, doi: 10.6038/cjg2021O0478.

Terzaghi K., Peck R. and Mesri G.; 1996: *Soil mechanics in engineering practice*. *3rd ed*. John Wiley & Sons, Hoboken, NJ, USA, 592 pp.

Toksöz M., Cheng C. and Timur A.; 1976: *Velocities of seismic waves in porous rocks*. Geophysics, 41, 621–645, doi: 10.1190/1.1440639.

Tran D., Raim C. and Sondergeld C.; 2008: *Changes in crack aspect-ratio concentration from heat treatment: a comparison between velocity inversion and experimental data*. Geophysics, 73, 123-132, doi: 10.1190/1.2928848.

Tsang C., Neretnieks I. and Tsang Y.; 2015: *Hydrologic issues associated with nuclear waste repositories*. Water Resour. Res., 51, 6923-6972, doi: 10.1002/2015WR017641.

Verwer K., Eberli G. and Wefer R.; 2011: *Effect of pore structure on electrical resistivity in carbonates*. AAPG Bulletin, 95, 175-190, doi: 10.1306/06301010047.

Voigt W.; 1928: *Lehrbuch der Kristallphysik*. Bibliotheca Mathematica Teubneriana, Band 12, Stuttgart, Germany, 739 pp., doi: 10.1007/978-3-663-15884-4.

Weger R., Eberli G., Baechle G., Massaferro J. and Sun Y.; 2009: *Quantification of pore structure and its effect on sonic velocity and permeability in carbonates*. AAPG Bulletin, 93, 1297–1317, doi: 10.1306/05270909001.

Whitaker S.; 1986: *Flow in porous media I: a theoretical derivation of Darcy's law*. Transp. Porous Media, 1, 3–25, doi: 10.1007/BF01036523.

Xie S., Cheng Q., Ling Q., Bing L., Bao Z. and Ping F.; 2010: *Fractal and multifractal analysis of carbonate pore-scale digital images of petroleum reservoirs*. Mar. Pet. Geol., 27, 476-485, doi: 10.1016/j.marpetgeo.2009.10.010.

Xiong F., Sun W., Ba J. and Carcione J.; 2020: *Effects of fluid rheology and pore connectivity on rock permeability based on a network model*. J. Geophys. Res.: Solid Earth, 125, 15 pp., doi: 10.1029/2019JB018857.

Xiong F., Gan L., Sun W. and Yang H.; 2021: *Characterization of reservoir permeability and analysis of influencing factors in fracture-pore media*. Chin. J. Geophys., 64, 279-288, doi: 10.6038/cjg2021N0175.

Yan F., Han D., Yao Q. and Zhao L.; 2014: *Prediction of seismic wave dispersion and attenuation from ultrasonic velocity measurements*. Geophysics, 79, 1-8, doi: 10.1190/geo2013-0416.1.

Yang Z. and Dong M.; 2017: *A new measurement method for radial permeability and porosity of shale*. Petroleum Research, 2, 178–185, doi: 10.1016/j.ptlrs.2017.07.004.

Yin H., Zhao J., Tang G., Zhao L., Ma X. and Wang S.; 2017: *Pressure and fluid effect on frequency-dependent elastic moduli in fully saturated tight sandstone*. J. Geophys. Res.: Solid Earth, 122, 8925-8942, doi: 10.1002/2017JB014244.

Yu B., Zhang D., Xu B., Li M., Liu C. and Xiao W.; 2022: *Experimental study on the effective stress law and permeability of damaged sandstone under true triaxial stress*. International Journal of Rock Mechanics and Mining Sciences, 157, 15 pp., doi: 10.1016/j.ijrmms.2022.105169.

Yu J., Mu K., Li H., Cai Y. and Zhang Y.; 2014: *The porosity distribution mesoscopic simulation analysis of the permeability evolution property of sandstone*. Engineering Mechanics, 34, 124-131, doi: 10.6052/j.issn.1000-4750.2013.05.0443.

Yu J., Yao W., Duan K., Liu X. and Zhu Y.; 2020: *Experimental study and discrete element method modeling of compression and permeability behaviors of weakly anisotropic sandstones*. Int. J. Rock Mech. Min. Sci., 134, 14 pp., doi: 10.1016/j.ijrmms.2020.104437.

Zhang L., Ba J. and Carcione J.M.; 2021: *Wave propagation in infinituple-porosity media*. J. Geophys. Res.: Solid Earth, 126, 19 pp., doi: 10.1029/2020JB021266.

Zhang L., Ba J., Li C., Carcione J.M. and Zhou F.; 2022: *Joint inversion of the unified pore geometry of tight sandstones based on elastic and electrical properties*. J. Pet. Sci. Eng., 219, 15 pp., doi: 10.1016/j. petrol.2022.111109.

Zhang Y. and Toksöz M.; 2012: *Impact of the cracks lost in the imaging process on computing linear elastic properties from 3D microtomographic images of Berea sandstone*. Geophysics, 77, 95-104, doi: 10.1190/ geo2011-0126.1.

Zhou H., Yu X., Chen C., Lu S., Wu L. and Zeng L.; 2019: *Pore-scale lattice Boltzmann modeling of solute transport in saturated biochar amended soil aggregates*. J. Hydrol., 577, 8 pp., doi: 10.1016/j.jhydrol.2019.123933.

Corresponding author: Jing Ba
                           School of Earth Sciences and Engineering, Hohai University
                           8 West Focheng Road, Nanjing, Jiangsu 211100, China
                           Phone: 86-2583787234; e-mail: jba@hhu.edu.cn